

# Liquid Structure with Nano-Heterogeneity Promotes Cationic Transport in Concentrated Electrolytes

Oleg Borodin,<sup>\*,†,§</sup> Liumin Suo,<sup>‡,§,¶</sup> Mallory Gobet,<sup>||</sup> Xiaoming Ren,<sup>†</sup> Fei Wang,<sup>†,‡</sup> Antonio Faraone,<sup>⊥</sup> Jing Peng,<sup>||</sup> Marco Olguin,<sup>†</sup> Marshall Schroeder,<sup>†</sup> Michael S. Ding,<sup>†,||</sup> Eric Gobrogge,<sup>†</sup> Arthur von Wald Cresce,<sup>†</sup> Stephen Munoz,<sup>||</sup> Joseph A. Dura,<sup>⊥</sup> Steve Greenbaum,<sup>||</sup> Chunsheng Wang,<sup>\*,‡,||</sup> and Kang Xu<sup>\*,†</sup>

<sup>†</sup>Electrochemistry Branch, Sensor and Electron Devices Directorate, U.S. Army Research Laboratory, Adelphi, Maryland 20783, United States

<sup>‡</sup>Key Laboratory for Renewable Energy, Beijing Key Laboratory for New Energy Materials and Devices, Beijing National Laboratory for Condensed Matter Physics, Institute of Physics, Chinese Academy of Sciences, School of Physical Sciences, University of Chinese Academy of Sciences, Beijing 100190, China

<sup>§</sup>Department of Chemical and Biomolecular Engineering, University of Maryland, College Park, Maryland 20742, United States

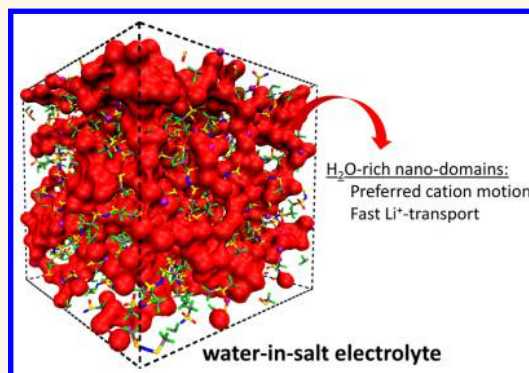
<sup>||</sup>Department of Physics and Astronomy, Hunter College, City University of New York, New York, New York 10065, United States

<sup>⊥</sup>NIST Center for Neutron Research, National Institute of Standards and Technology, Gaithersburg, Maryland 20899-6100, United States

## Supporting Information

**ABSTRACT:** Using molecular dynamics simulations, small-angle neutron scattering, and a variety of spectroscopic techniques, we evaluated the ion solvation and transport behaviors in aqueous electrolytes containing bis(trifluoromethanesulfonyl)imide. We discovered that, at high salt concentrations (from 10 to 21 mol/kg), a disproportionation of cation solvation occurs, leading to a liquid structure of heterogeneous domains with a characteristic length scale of 1 to 2 nm. This unusual nano-heterogeneity effectively decouples cations from the Coulombic traps of anions and provides a 3D percolating lithium–water network, *via* which 40% of the lithium cations are liberated for fast ion transport even in concentration ranges traditionally considered too viscous. Due to such percolation networks, superconcentrated aqueous electrolytes are characterized by a high lithium-transference number (0.73), which is key to supporting an assortment of battery chemistries at high rate. The in-depth understanding of this transport mechanism establishes guiding principles to the tailored design of future superconcentrated electrolyte systems.

**KEYWORDS:** aqueous electrolytes, batteries, molecular dynamics simulations, spectroscopy, conductivity



The electrolyte serves as the indispensable ion conductor and electron-insulator between the cathode and anode in all electrochemical devices. It forces the charge transfer to occur at electrode/electrolyte interfaces instead of directly between the cathode (oxidant) and anode (reductant), and its ability to conduct ions determines how fast the cell chemistry can proceed.<sup>1</sup> Traditionally, the design and formulation of electrolytes have centered around the salt concentrations where the maximum ion conductivity ( $\sigma_m$ ) occurs. This optimum concentration ( $C_{\sigma_m}$ ) is the result of the compromise between solution viscosity and population of ionic carriers.<sup>2</sup> For nonaqueous electrolytes,  $\sigma_m$  always occurs in the

dilute ranges near 1.0 m (m = mol/kg), while the higher solvating power of H<sub>2</sub>O, as characterized by both high dielectric constant ( $\epsilon = 78$  at 25 °C) and acceptor and donor numbers (AN = 54.8, DN = 18), shifts  $\sigma_m$  toward higher concentrations. Thus, in practical electrochemical devices, the salt concentrations are almost always around 1.0 M (M = mol/L) for nonaqueous electrolytes and below 5 m in aqueous electrolytes.

Received: August 9, 2017

Accepted: October 10, 2017

Published: October 10, 2017

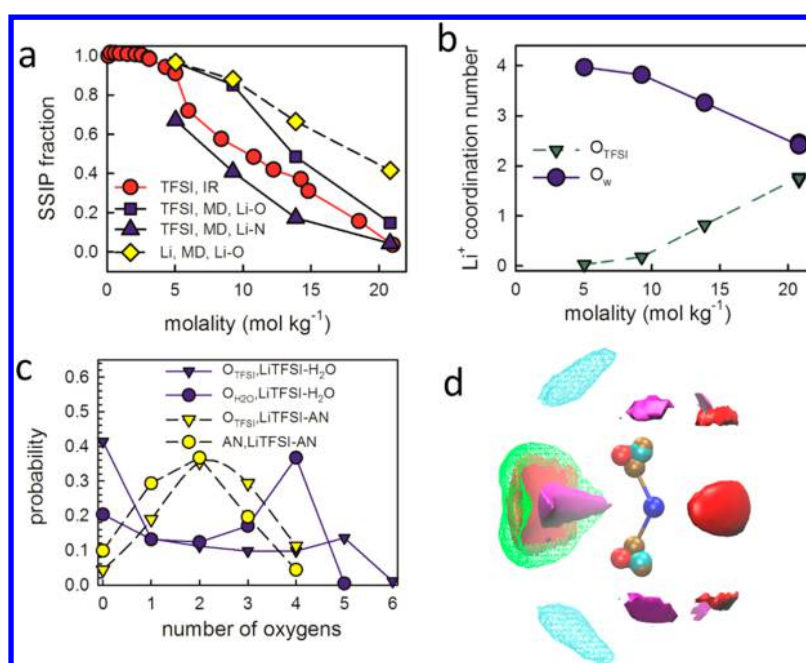


**Figure 1.** Solvation: (a) Fraction of the solvent-separated and free TFSI<sup>-</sup> anions as a function of salt concentration as derived from the S=O band stretch vibrational mode in FTIR and MD simulations using two different criteria for SSIP formation in MD simulations: (1) SSIP is formed if there is no Li<sup>+</sup> within a range of 5 Å from N(TFSI), (2) SSIP is formed if there is no Li within 2.7 Å from any of O(TFSI); a fraction of the solvent-separated Li<sup>+</sup> is also shown; (b) Li<sup>+</sup> cation coordination numbers from MD simulations using a 2.7 Å cutoff for the first shell; and (c) probability of finding a specific number of oxygens from TFSI, H<sub>2</sub>O, or nitrogen atoms from acetonitrile (AN) in the Li<sup>+</sup> first coordination shell for LiTFSI in H<sub>2</sub>O and LiTFSI in AN from MD simulations at solvent:Li = 2.67. (d) Isosurfaces of water oxygen (red solid,  $\rho/\rho_{\text{bulk}} = 5$ , where  $\rho$  is local density and  $\rho_{\text{bulk}}$  is bulk average density), oxygen of TFSI (green mesh,  $\rho/\rho_{\text{bulk}} = 2.5$ ), fluorine of TFSI (cyan mesh,  $\rho/\rho_{\text{bulk}} = 2$ ), and Li<sup>+</sup> (purple solid,  $\rho/\rho_{\text{bulk}} = 12$ ) for 21 m LiTFSI in H<sub>2</sub>O at 298 K. Average atom positions of the flexible TFSI are shown, resulting in a somewhat collapsed structure of the -SO<sub>2</sub>-CF<sub>3</sub> group. TFSI colors: N (blue), O (red), F (cyan), S and C (brown).

By this tradition, excessively concentrated electrolytes were unfavorable due to undesirable properties such as lower ion conductivity, narrower liquid range, and higher viscosity. These disadvantages make it difficult for the electrolyte to fully access the porosity of both the electrodes and the separators and incapable of supporting the cell reactions with sufficient mass flow and severely restrict the service temperature of the devices. It should be mentioned that, by this “conductivity-centric” principle, only overall ion conductivity was considered, while the importance of ion-transference number ( $t_+$  or  $t_-$ ), which stands for the portion of current carried by a certain ion species,<sup>1</sup> was often overlooked. For a given cell chemistry, however, only the ionic current provided by a specific ionic species (such as Li<sup>+</sup> for lithium batteries) is meaningful, while those contributed by the migration of other ionic species is considered parasitic and responsible for concentration polarizations within the cell.

In recent years this “conductivity-centric” custom was breached by a series of efforts in the field of batteries when researchers sought “unusual” properties that were otherwise unavailable at lower salt concentrations to benefit the electrochemical performances of various battery chemistries. This trend was represented by the pioneering polymer-in-salt concept of Angell *et al.*, who attempted to decouple ion transport from mechanical strength of polymer materials,<sup>3,4</sup> followed by Abe and Ogumi *et al.*,<sup>5,6</sup> who found that the intercalation chemistry of graphite could be quite unexpectedly supported by propylene carbonate (PC) solvent as long as salt was used at sufficient concentrations (~5 M), and Watanabe *et al.*, who discovered that volatile ether-based electrolytes gained thermal stability at high salt concentrations,<sup>7</sup> while demonstrat-

ing solubility/insolubility toward sulfur active materials.<sup>8–10</sup> These approaches were further refined by Yamada *et al.*, who used unconventional solvents to achieve unusual interfacial properties on a graphite anode<sup>11</sup> and high-voltage cathode<sup>12</sup> when lithium salts were used at superconcentrations. Solvent concentrations also greatly influenced Al current collector corrosion.<sup>13,14</sup> This was carried to its extreme when Suo *et al.* dissolved up to 21 m lithium salt (lithium bis(trifluoromethane sulfonyl)imide, LiTFSI) and successfully expanded the electrochemical stability window of aqueous electrolytes from 1.23 V to nearly 3.0 V,<sup>15</sup> leading to a paradigm shift in aqueous electrolytes, which have been demonstrated with an assortment of battery chemistries with exceptional performances by numerous research groups.<sup>15–23</sup>

The superconcentrated aqueous electrolyte reported therein, along with its improved variations reported later on,<sup>17,24</sup> also presents an unexplored frontier, where little is known about how ions interact with solvent molecules and with each other or how they participate in transport. In this work, combining computational and complementary characterization techniques, we explore this frontier and describe how a discovered nanoscale heterogeneity influences a range of structural and dynamic properties in this class of aqueous electrolytes.

## RESULTS AND DISCUSSION

**Ion Solvation.** It has been well established that cations are well solvated while anions remain relatively free in diluted nonaqueous electrolytes.<sup>25–27</sup> This is partially caused by the fact that the formal charges are usually more delocalized on the anion rather than on the cation, but more importantly, the typical nonaqueous solvent molecules, regardless of chem-

istry—ethers, esters, sulfones, or nitriles—are better electron donors than acceptors, as structurally their negative termini are more readily accessible than positive termini (Figure S1a). However, this “cation preference” would be significantly weakened in aqueous solutions, as H<sub>2</sub>O molecules are bipolar in nature and solvate both cations and anions effectively (Figure S1b). According to quantum chemistry (QC) calculations, the total binding energy for Li<sup>+</sup>(H<sub>2</sub>O)<sub>4</sub>, −103 kcal/mol,<sup>15</sup> is smaller than for bipolar solvents: Li<sup>+</sup>(AN)<sub>4</sub> with a binding energy of −117.5 kcal/mol<sup>28</sup> and −122 kcal/mol for Li<sup>+</sup> coordinated by cyclic carbonates, as shown in Figure S2.<sup>29</sup> Yet, salt dissociation is higher in H<sub>2</sub>O due to its bipolar character and the more effective solvation of anions. On the other hand, the interaction between cations and anions depends critically on the salt concentration, as the number of solvent molecules available to solvate cations or anions determines whether a counterion enters into the primary solvation sheath of each other, forming the so-called contact ion pair (CIP). As the concentration of LiTFSI increases from 1.0 m to 21 m, the H<sub>2</sub>O-to-salt molar ratio decreases from 55.6 to 2.6, resulting in the coexistence of various ionic species from solvent-separated ion pairs (SSIPs) to CIPs and ionic aggregates (AGGs). Fourier-transformed infrared (FTIR) measurements conducted on the LiTFSI–H<sub>2</sub>O system track such changes in the stretching vibrational mode of the S=O band (Figure S3). Applying principal component analysis, we were able to deconvolute the three major components (free TFSI anion, SSIPs, and AGGs consisting of Li<sup>+</sup> and TFSI<sup>−</sup>), whose molar distribution is shown as a function of LiTFSI concentration (Figure 1a). A similar distribution of ionic species was also obtained from the symmetric stretching of the S–N bond, which includes in-plane (1132–1139 cm<sup>−1</sup>) and the out-of-plane (1143–1149 cm<sup>−1</sup>), or the antisymmetric stretching of the S–O bond, which includes in-plane (1352–1355 cm<sup>−1</sup>) and out-of-plane (1330–1336 cm<sup>−1</sup>), each of which were measured and analyzed (Figures S3 and S4). Based on this analysis, minimal CIP formation is observed below 5 m, while highly concentrated solutions yield a high fraction of CIPs and AGGs. This intensified association between Li<sup>+</sup> and TFSI<sup>−</sup> constitutes the foundation for the formation of a LiF-rich interphase on the anode above 1.5 V *vs* Li/Li<sup>+</sup> as a result of the salt reduction and is essential for expanding the electrochemical stability window.<sup>15,30</sup>

MD simulations also predicted little CIP formation at 5 m and a similar decrease in the fraction of SSIPs with increasing salt concentrations. Two definitions of the Li–TFSI bond formation are utilized here: the first one uses the distance of the minima after the first Li–N(TFSI) peak of 5.0 Å, while the second uses the position of the first Li–O(TFSI) peak and counts the Li–O(TFSI) ion pair being formed if any of the TFSI-oxygens are bound to a Li<sup>+</sup> (see Figures S5 for the radial distribution functions). The Li–O(TFSI)-based definition does not include the Li⋯TFSI CIPs, where the Li<sup>+</sup> cation is bound to the CF<sub>3</sub> groups (see Figure S6a,b); thus it overestimates the solvent-separated TFSI anions. The Li–N(TFSI) definition, on the other hand, counts all the Li⋯TFSI bonds including most of the Li⋯F(TFSI) contacts but in some cases incorrectly counts the compact SSIPs as CIPs, as shown in Figure S6c. Thus, the latter definitions provide a lower bound estimate of the fraction of the solvent-separated TFSI anions shown in Figure 1a. The experimentally determined fraction of the solvent-separated TFSI<sup>−</sup> shown in Figure 1a is in excellent agreement with the MD simulation predictions, as the two

definitions used for the solvent-separated TFSI anions envelop the experimentally derived curve. Unlike FTIR, which can only detect the TFSI anion, MD also probes the association behaviors of the Li<sup>+</sup> cations, as shown in Figure 1a. An important insight generated by MD that will be of high significance to ion transport is that, according to the MD predictions, the fraction of SSIP Li<sup>+</sup> is significantly higher than the fraction of SSIP TFSI<sup>−</sup>. This result suggests that a surprisingly high fraction of Li<sup>+</sup> remains “free”, perhaps in the form of Li<sup>+</sup>(H<sub>2</sub>O)<sub>4</sub>, and that these clusters are complemented by negative anion-rich domains such as Li<sup>+</sup>(TFSI<sup>−</sup>)<sub>x</sub> with *x* > 1.

The Li<sup>+</sup>-solvation sheath details are analyzed from MD simulations. The Li<sup>+</sup> primary sheath has a radius of 2.7 Å, which corresponds to the location of the minimum after the first peak in the Li–O<sub>H<sub>2</sub>O</sub> radial distribution function (see Figure S5). We found that in solutions with lower concentration (<5 m) Li<sup>+</sup> is mainly solvated by four H<sub>2</sub>O molecules in its first coordination shell (Figure 1b), which is consistent with the neutron scattering results for other “dilute” salts.<sup>31,32</sup> Contact ion pairs start to form within the 5–10 m concentration range, and the trend continues with the increase in salt concentrations, resulting in a very aggregated solution at 21 m with each Li<sup>+</sup> coordinated by approximately two oxygens from TFSI and two oxygens from H<sub>2</sub>O in its first solvation sheath. However, the average coordination numbers do not give the full picture of the distribution of H<sub>2</sub>O and TFSI around Li<sup>+</sup>. A closer look is revealed by the analysis of the distributions of various environments shown in Figure 1c. Even though each Li<sup>+</sup> is coordinated by 1.75 TFSI oxygens on average, a very high fraction (40%) of the Li<sup>+</sup> actually exist as SSIPs with no TFSI in their first coordination shell at all. Specifically, the Li<sup>+</sup> ions prefer either (1) to be fully solvated by four H<sub>2</sub>O molecules or (2) to participate in the formation of the LiTFSI aggregates so that each Li<sup>+</sup> is surrounded by four oxygens of TFSI, rather than an even division of H<sub>2</sub>O molecules and TFSI around each Li<sup>+</sup>.

Such a solvation disproportionation is uncommon in nonaqueous electrolytes such as the LiTFSI–acetonitrile (AN) system, which was selected as a representative nonaqueous electrolyte due to multiple similarities between AN and H<sub>2</sub>O that include large dipole moments (3.92 D for AN *vs* 1.8546 D for H<sub>2</sub>O) and high dielectric constant (36.8 for AN *vs* 78 for H<sub>2</sub>O). Despite similar average coordination numbers (1.78 AN and 2.26 O(TFSI) per Li<sup>+</sup>) with 21 m LiTFSI–H<sub>2</sub>O, the primary Li<sup>+</sup>-solvation sheath in LiTFSI–AN consists of two solvents and two O(TFSI) as the most probable configuration, with only a small fraction (10%) of SSIP Li<sup>+</sup>. This even distribution of AN molecules and TFSI leads to a more homogeneous Li<sup>+</sup> environment, where the cation and anion are expected to be intimately coupled. In sharp contrast, the “disproportionation” in solvation behaviors by H<sub>2</sub>O and TFSI would certainly create a rather inhomogeneous local Li<sup>+</sup> environment, and the difference in solvation sheath structures is expected to result in dramatically different ion transport as well as interphasial behaviors.

The structure of the TFSI<sup>−</sup> shell is examined in Figure 1d by plotting the isosurfaces of 3D distributions of species around the TFSI<sup>−</sup> anion. The Li<sup>+</sup> cation primarily binds to TFSI oxygens and is coordinated by oxygens from the other TFSI or water, as also shown in Figure S12. Water oxygens often coordinate the TFSI<sup>−</sup> anion on the side opposite the Li<sup>+</sup> cation in addition to coordinating the Li<sup>+</sup> cations. The Li<sup>+</sup> cation binding to F(TFSI) atoms is less probable than binding to

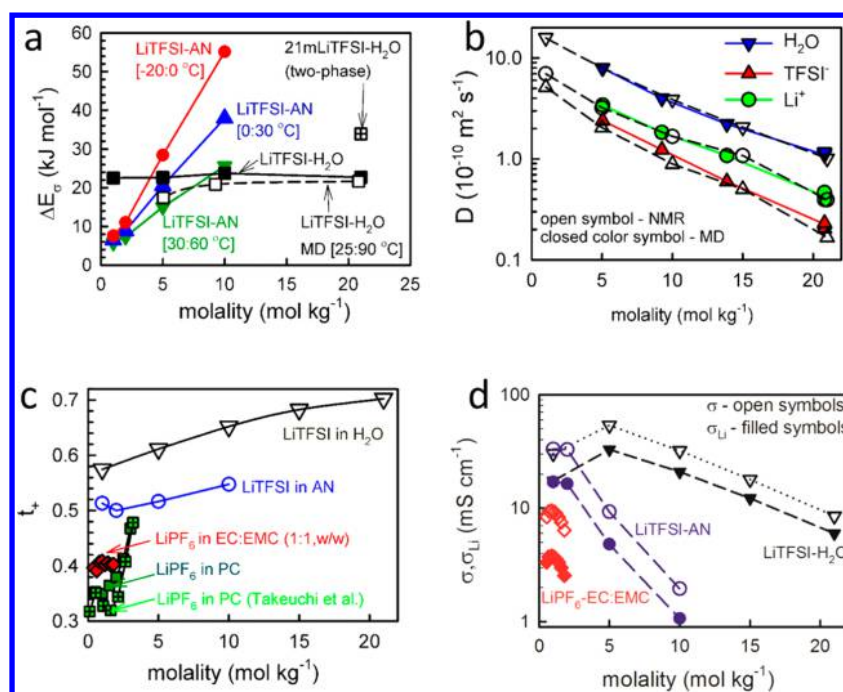


**Figure 2.** Ion transport: (a) Comparison of activation energies of LiTFSI–AN and LiTFSI–H<sub>2</sub>O as a function of salt concentrations from experiments and for LiTFSI–H<sub>2</sub>O from MD simulations; (b) ion and H<sub>2</sub>O self-diffusion coefficients for the LiTFSI–H<sub>2</sub>O electrolyte from MD simulations at 25 °C and pfg-NMR experiments at 20 °C; (c) the Li<sup>+</sup>-transference number as measured by pfg-NMR for the electrolytes with one primary solvation group: for LiTFSI in H<sub>2</sub>O at 20 °C, LiPF<sub>6</sub> in PC, EC:EMC (1:1 wt %), and LiTFSI–AN at 25 °C; data from Takeuchi *et al.* for PC–LiPF<sub>6</sub> at 25 °C are also shown;<sup>43</sup> (d) conductivity ( $\sigma$ ) and the Li<sup>+</sup> contribution to conductivities ( $\sigma_{Li}$ ) for LiTFSI–H<sub>2</sub>O, LiTFSI–AN, and LiPF<sub>6</sub>–EC:EMC (1:1 wt/wt).

O(TFSI). Finally, the relatively hydrophobic –CF<sub>3</sub> group approaches the –CF<sub>3</sub> groups of the other TFSI the closest.

**Ion Transport.** In both nonaqueous and aqueous electrolytes a maximum in conductivity ( $\sigma_m$ ) occurs as the compromise between solution viscosity and population of ionic carriers. At concentrations higher than  $C_{\sigma,m}$ , increasing ion aggregation results in a decrease of available free ions that can participate in conducting current, while increasing Coulombic frictions among cation, anion, and solvent molecules simultaneously creates additional viscous drag to any moving species, with or without charge. An apparent difference between aqueous and nonaqueous electrolytes rests with the solubility of salts therein.<sup>1</sup> The bipolar nature of H<sub>2</sub>O enables it to be very effective at coordinating with both cations and anions, which typically results in a much higher  $\sigma_m$  and at a higher  $C_{\sigma,m}$  as compared with the nonaqueous solvent molecules of esters, ethers, sulfones, or nitriles, which are polar but are usually only nucleophilic. The combination of this excellent solvation power of H<sub>2</sub>O and the excellent solubility of LiTFSI in it, enabled by its well-delocalized anion structure, makes it possible to create an extremely concentrated aqueous electrolyte, where the salt concentration can reach 21 m. In this superconcentrated LiTFSI–H<sub>2</sub>O system, despite its high viscosity (32 mPa s), the ionic conductivity ( $\sim 8$  mS/cm at 25 °C)<sup>15,33</sup> is comparable to what typical nonaqueous electrolytes can offer (*e.g.*,  $\sim 10$  mS/cm at 25 °C for LiPF<sub>6</sub> in EC/EMC, 30:70). For comparison, at 60 °C, the LiTFSI–H<sub>2</sub>O conductivity is also about a factor of 2 higher than conductivity for LiTFSI–AN, one of the most conductive nonaqueous systems. Numerous aqueous cell chemistries have been found to be effectively supported by this electrolyte or its variations at high rates,<sup>15,24,34</sup> some of which even the nonaqueous electrolytes fail to rival.

In a simple comparison between the reciprocal temperature dependences of ion conductivities (Figure S7), one would immediately conclude that the LiTFSI–H<sub>2</sub>O system is characterized by strong Arrhenius behavior even at the extreme salt concentration of 21 m, while LiTFSI–AN displayed typically a non-Arrhenius feature that is well described by the empirical Vogel–Fulcher–Tamman (VFT) relation, as most nonaqueous electrolytes investigated thus far. The deviations from the Arrhenius behavior only occurred in the LiTFSI–H<sub>2</sub>O system around 0 and 20 °C, when partial crystallization of either H<sub>2</sub>O or LiTFSI leads to two-phase coexistence.<sup>35</sup> Surprisingly, significant conductivity is still maintained in the two-phase region at lower temperatures, making this electrolyte rather durable for supporting battery operations even below its melting point.

Detailed analyses were carried out to identify the activation energies associated with ion transport in each electrolyte. Due to the nonlinear nature of the nonaqueous system, the temperature dependence of conductivity could be divided into three temperature regions, *i.e.*, from  $-20$  to  $\sim 0$  °C, from 0 to  $\sim 30$  °C, and from 30 to  $\sim 60$  °C (Figure S7). Each section displays strongly concentration-dependent activation energies, as shown in Figure 2a, with the concentrated electrolytes associated with the highest activation energy (30–50 kJ/mol), an indication of how difficult it is to move cations and anions free from their individual Coulombic cages. Thus, we speculate that in nonaqueous media at high salt concentrations, Li<sup>+</sup> movement is expected to be intimately coupled with TFSI<sup>−</sup>. Similar increase of the activation energy with concentration has been observed in 1,3-dioxolane (DOL): dimethoxyethane (DME) doped with LiTFSI,<sup>9</sup> glymes–LiTFSI,<sup>36</sup> AN doped with LiTFSI, LiPF<sub>6</sub>, LiClO<sub>4</sub>, LiBF<sub>4</sub>, and LiCF<sub>3</sub>CO<sub>2</sub>,<sup>37</sup> and mixtures of carbonates with LiPF<sub>6</sub> or LiBF<sub>4</sub> salt.<sup>38</sup> In sharp

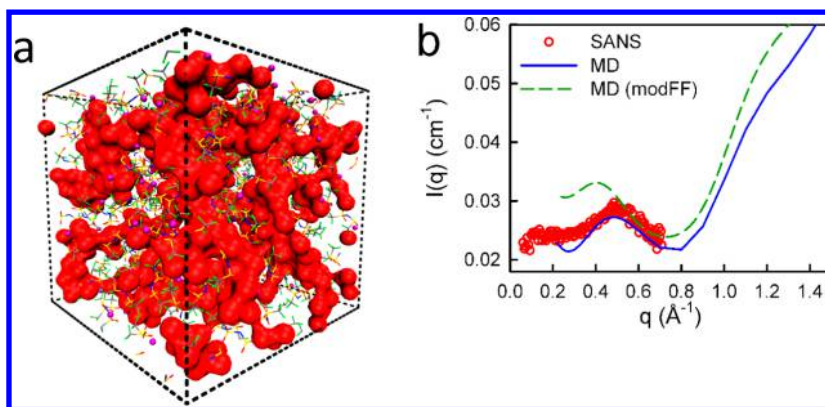


**Figure 3.** Liquid structure of nano-heterogeneity: (a) 3D snapshot showing an interconnected H<sub>2</sub>O domain in red and TFSI anions as wireframe from MD simulations of 21 m LiTFSI–H<sub>2</sub>O at 298 K; (b) structure factor from SANS experiments and MD simulations for 21 m LiTFSI in D<sub>2</sub>O. Results from the MD simulations using a modified force field (modFF) with the weaker Li<sup>+</sup>–O(H<sub>2</sub>O) interaction are also shown and denoted as modFF.

contrast, over the entire concentration range, the aqueous electrolytes demonstrated a concentration independence of the activation energies, which remain at a constant low value of ~20 kJ/mol even at superconcentration. As predicted in Figure 1c, a very substantial fraction of the solvent-separated Li<sup>+</sup>(H<sub>2</sub>O)<sub>4</sub> is expected to exist, which facilitates the Li<sup>+</sup> diffusion through a framework consisting of TFSI and yields a noticeably different transport mechanism in LiTFSI–H<sub>2</sub>O. It is this “solvation disproportionation” in ion aggregation that is responsible for the fast ion conduction even at very high salt concentration. Interestingly, analysis of ion transport in LiTFSI–H<sub>2</sub>O using the so-called Walden rule, as shown in Figure S8 as the dependence of molar ion conductivity on electrolyte fluidity (inverse viscosity), indicated that increasing viscosity and decreasing fluidity brought data slightly closer to the ideal line, indicating decoupling of ionic motion as salt concentration increases.

The diffusivities of <sup>1</sup>H, <sup>7</sup>Li, and <sup>19</sup>F were measured separately by pfg-NMR as a function of salt concentration, which correspond to the movement of solvent molecules (H<sub>2</sub>O), cations (Li<sup>+</sup>), and anions (TFSI<sup>−</sup>), respectively. Three representative nonaqueous electrolytes, LiTFSI–AN, LiPF<sub>6</sub>–PC, and LiPF<sub>6</sub>–ethylene carbonate/ethylmethyl carbonate (EC/EMC) (1:1), were selected for comparison. Figure 2b compares these diffusivities in LiTFSI–H<sub>2</sub>O at 20 °C, along with a data set provided by MD simulations at 25 °C, and the apparent transference number of Li<sup>+</sup> (*t*<sup>+</sup>) is evaluated according to

$$t^+ = \frac{D_{\text{Li}^+}}{D_{\text{Li}^+} + D_{\text{TFSI}^-}} \quad (1)$$

where  $D_{\text{Li}^+}$  and  $D_{\text{TFSI}^-}$  represent cation and anion diffusivities, respectively. Figure 2c summarizes the concentration dependence of *t*<sup>+</sup> for LiTFSI–H<sub>2</sub>O along with these nonaqueous counterparts. The superconcentrated LiTFSI–H<sub>2</sub>O at 21 m stands out with a *t*<sup>+</sup> of 0.70 and 0.73 at 20 and 30 °C, respectively, as shown in Tables S2 and S3, far above what typical nonaqueous electrolytes could offer. On the other hand, a comparable *t*<sup>+</sup> of 0.6–0.7 has been also described in a few superconcentrated electrolytes based on ethers, including LiTFSI–triglyme or LiTFSI–1,3-dioxalane/dimethoxyethane<sup>9,39–41</sup> and sulfolane/ethyl acetate/LiBF<sub>4</sub> electrolytes.<sup>42</sup> After converting overall ion conductivities ( $\sigma$ ) into Li<sup>+</sup> conductivities ( $\sigma_{\text{Li}}$ ), the superconcentrated LiTFSI–H<sub>2</sub>O at

21 m is clearly a much better electrolyte to support Li-ion chemistries (Figure 2d), with a  $\sigma_{\text{Li}}$  of 7.3 mS/cm in comparison with 3.7 mS/cm for the typical nonaqueous electrolyte 1.0 m LiPF<sub>6</sub>–EC/EMC (50:50), despite the similar overall conductivities for both (~10 mS/cm).

It is well known that cation-transference numbers in typical nonaqueous electrolytes are seldom above 0.50<sup>1,2,44,45</sup> and are often even lower for nonconcentrated aqueous electrolytes: within 0.2 to 0.45 for the LiCl, LiClO<sub>4</sub>, and LiCF<sub>3</sub>SO<sub>3</sub>-based aqueous electrolytes.<sup>46</sup> This under-representation of the cation in ion transport current implies the inability of electrolytes to maintain sufficient mass flow to support a cell chemistry involving the cation, especially under high current, where severe concentration polarization occurs. A typical example is the Li-ion battery, which suffers from a series of harmful parasitic reactions at high C-rates, such as Li metal deposition due to Li<sup>+</sup> depletion at electrolyte/electrode surfaces and excessive electrolyte decompositions. In this sense, a preferred cation transport would significantly improve the electrochemical performances of batteries by minimizing the movement of the ions that do not participate in the intercalation or conversion reactions at electrodes.

Closer examination of measured diffusivities reveals that, across the entire concentration range, H<sub>2</sub>O molecules are the most mobile species, followed by Li<sup>+</sup>, while TFSI<sup>−</sup> are the least mobile (Figure 2b). At concentrations higher than 5 m, the ratio among the diffusivities of H<sub>2</sub>O, Li<sup>+</sup>, and TFSI<sup>−</sup> becomes approximately constant, indicating that a connection exists between the solvent and ion movements. A combination of pfg-NMR and conductivity measurements allows us to determine the so-called ionicity using eqs 2 and 3, which defines  $\alpha_{\text{d}}$ , which reflects the degree of uncorrelated ionic motion:

$$a_{\text{d}} = \frac{\sigma}{\sigma_{\text{uncorr}}} \quad (2)$$

$$\sigma_{\text{uncorr}} = \frac{e^2}{k_{\text{B}}T} (n_+ D_+ + n_- D_-) \quad (3)$$

where  $e$ ,  $n_+$  and  $n_-$ ,  $k_{\text{B}}$ , and  $T$  are electron charge, number densities of Li<sup>+</sup> and TFSI<sup>−</sup> in the material, Boltzmann constant, and temperature, respectively. Interestingly, in accord with the Walden plot, ionicity was found to remain relatively steady in the region of 0.64 to 0.76 as salt concentration increases (see Figure S9), indicating that even in the very concentrated regime

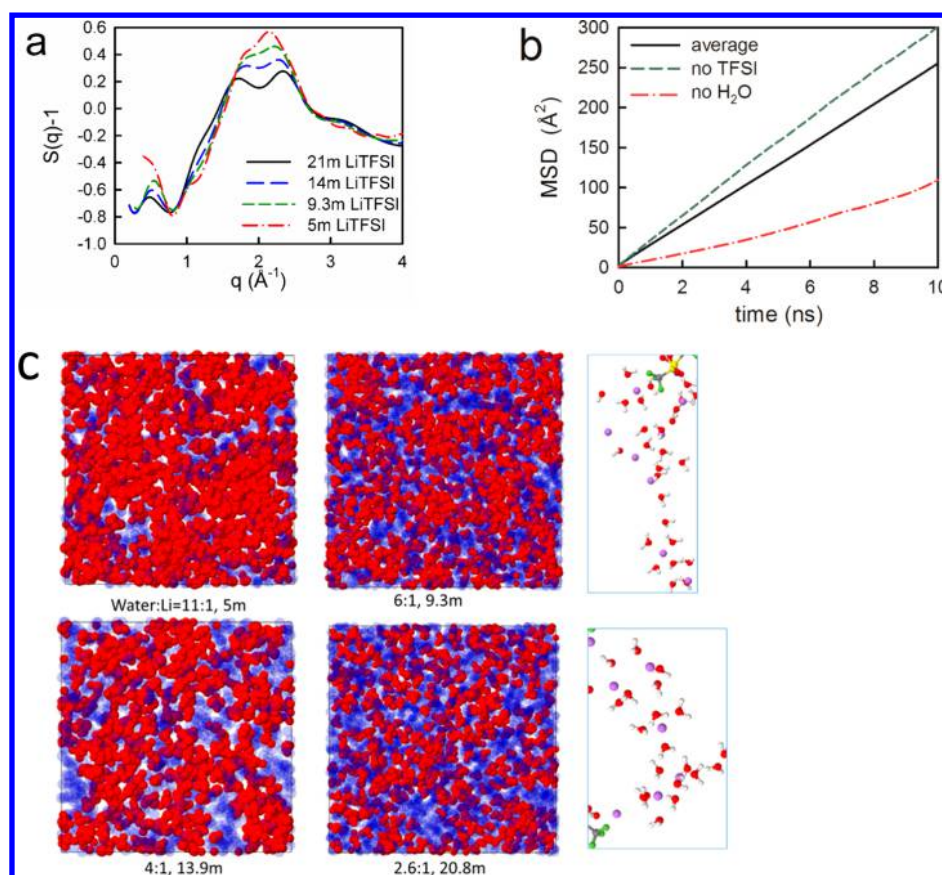


**Figure 4.** (a) Neutron-weighted structure factor  $S(q)$  for LiTFSI in  $\text{D}_2\text{O}$  as a function of salt concentration from MD simulations. (b) The  $\text{Li}^+$  cation mean-squared displacements (MSDs) for 21 m LiTFSI– $\text{H}_2\text{O}$  for all  $\text{Li}^+$  cations (average MSD) and the  $\text{Li}^+$  cations that do not have O(TFSI) or  $\text{O}_w$  within 2.7  $\text{\AA}$ . (c) Snapshots of LiTFSI– $\text{H}_2\text{O}$  MD (APPLE&P) simulations at 298 K with  $\text{H}_2\text{O}$  molecules shown in red and LiTFSI in blue and two representative  $\text{Li}^+(\text{H}_2\text{O})_n$  clusters extracted from simulations at 21 m (on the right).

where one should expect significant cation–anion interactions, the movements of  $\text{Li}^+$  and  $\text{TFSI}^-$  are only weakly correlated. Similar values (0.6 to 0.7) were also observed in superconcentrated LiTFSI–triglyme.<sup>41</sup> Temperature dependence of  $\alpha_d$  as derived from MD simulations showed that it decreases slightly from 0.7 to 0.45 as the temperature increased from 298 K to 363 K for 21 m, implying that at this high salt concentration the ion dynamic correlation would increase with increasing temperature. However, at lower salt concentrations,  $\alpha_d$  would remain largely unchanged.

**Structure of Nano-heterogeneity.** The solvation disproportionation, the uneven distribution of  $\text{H}_2\text{O}$  and TFSI with each  $\text{Li}^+$ , the nearly constant activation energy, the preferred  $\text{Li}^+$  transport, and the degree of uncorrelated cation and anion movements suggest that an unexpected liquid structure may have formed in the superconcentrated aqueous electrolytes. This structure, differing from more conventional diluted aqueous/nonaqueous analogues, immobilizes the anion in some manner and frees a significant portion of cations from the Coulombic traps of their anions. The promoted fast cation transport effectively supported various cell chemistries at high C-rates.<sup>15,17,24</sup> Although researchers started suspecting unusual liquid structures arising in the superconcentration realm of nonaqueous electrolytes,<sup>47</sup> the salt concentrations therein (often <5 m) were not high enough to make these behaviors pronounced enough to be unambiguous, and direct evidence was never presented.

Based on MD simulation results presented above, an overall picture of matter distribution can be generated on a molecular level. We have observed that in the 21 m LiTFSI– $\text{H}_2\text{O}$  solution 40% of  $\text{Li}^+$  does not have any oxygen of TFSI in its first coordination shell, while 25% of  $\text{Li}^+$  does not have any  $\text{H}_2\text{O}$  in its primary solvation sheath (Figure 1c). The system does not phase-separate on a microscopic scale; however,  $\text{H}_2\text{O}$  is distributed nonhomogeneously and forms the interconnecting clusters shown in red in Figure 3a in a 3D rendering. The “anionic framework” as represented by wireframe regions appears to be structurally dissimilar to what exists in superionic glass/ceramics due to its long-range disorder and highly dynamic nature, as will be shown below. In a certain sense, these superconcentrated electrolytes should be viewed as an intermediate state transitioning from a diluted solution into an ionic liquid. Those 40% of  $\text{Li}^+$ , entirely coordinated by  $\text{H}_2\text{O}$  molecules, are expected to transport  $\text{Li}^+$  through the 3D percolating network shown in Figure 3a and are likely responsible for the unusually high  $\text{Li}^+$ -transference numbers. Importantly, the above nano-heterogeneity was not only observed in MD simulations but also confirmed experimentally with small-angle neutron scattering (SANS), in which  $\text{D}_2\text{O}$  was used in place of  $\text{H}_2\text{O}$  to enhance contrast due to a much larger coherent scattering length for deuterium than hydrogen. Figure 3b shows a structure factor from SANS that is precisely at the same position and has the same shape as predicted from MD simulations. A small low- $Q$  peak in the structure factor around

0.45 to 0.50  $\text{\AA}^{-1}$  indicates that a nanostructure is present on the scale of  $\sim 1.4$  nm.

MD simulations allow us to further prove the above link between the low- $Q$  peak and the proposed structure by artificially decreasing the fraction of  $\text{Li}^+(\text{H}_2\text{O})_4$  and examining how it influences the size of the nanodomains. MD simulations utilizing such a modified force field resulted in reducing the fraction of  $\text{Li}^+$  SSIP at 21 m from 40% for the original force field to 30%. This very small decrease in the  $\text{Li}^+$  SSIP population renders the low- $Q$  peak much less defined as shown in Figure 3b. Thus, a small change of the  $\text{Li}^+-\text{H}_2\text{O}$  interactions and the fraction of solvent-separated  $\text{Li}^+$  in MD simulations induces a significant change in the intermediate range structure, and the existence of a high fraction of the fully solvated  $\text{Li}^+(\text{H}_2\text{O})_4$  is important for creating a nanodomain structure in this electrolyte. Moreover, the sensitivity of the low- $Q$  peak toward the fraction of the solvent-separated  $\text{Li}^+$  cation provides additional evidence that the fraction of  $\text{Li}^+$  SSIP observed in MD simulations is accurate and highlights the high quality of the many-body polarizable APPLE&P force field used in simulations that also accurately predicted ion self-diffusion coefficients, conductivity, and viscosity.

The evolution of the nano-heterogeneity length scale with salt concentration was also analyzed as shown in Figure 4a. The peak increases in size with decreasing salt concentration up to 9.3 m and seems to completely disappear at 5 m. In accord with changes of the low- $Q$  peak, the nano-heterogeneity with a length scale of 1 to 2 nm seems to be more pronounced in the range of 9 to 14 m, while increasing the salt concentration to 21 m makes it less distinct. This trend becomes more visual in the snapshots of matter distribution (Figure 4b), where  $\text{H}_2\text{O}$  molecules and LiTFSI are shown in red and blue, respectively. Additional snapshots can also be seen in Figure S10. Analysis of the partial contributions to the structure factor shows that  $\text{D}_2\text{O}-\text{D}_2\text{O}$  correlations contribute the most to the low- $Q$  peak, as shown in Figure S13. Figure S14 shows that the low- $Q$  peak is largely absent in the deuterated AN-LiTFSI solutions because its solvation is dominated by  $\text{Li}^+(\text{AN})_n(\text{TFSI})_{4-n}$  ( $n = 2, 3, 4$ ) solvates that combine both AN and TFSI and a very small fraction of the  $\text{Li}^+(\text{AN})_4$  SSIP. Small and hydrophilic anions such as  $\text{Br}^-$  yielded structure factors without the low- $Q$  peak.<sup>48</sup> Poly(ethylene oxide) (PEO)-LiTFSI, on the other hand, formed the large-size  $\text{Li}^+(\text{ethylene oxide})_n$  ( $n = 5, 6$ ) solvates<sup>49</sup> that are often solvent separated from  $\text{TFSI}^-$ , resulting in the large intermediate range peak at 0.6  $\text{\AA}^{-1}$ , as shown in Figure S14, and was previously observed in neutron diffraction experiments.<sup>50</sup> In the TFSI-based room-temperature ionic liquids with small cations the low- $Q$  peak was observed at larger  $Q$  values,  $>0.8$   $\text{\AA}^{-1}$ , and was attributed to cation-cation and anion-anion correlations.<sup>51</sup>

The inhomogeneous structure of the superconcentrated LiTFSI- $\text{H}_2\text{O}$  system could be viewed as consisting of two independent but interpenetrating networks, one bearing excessive positive charge (*i.e.*,  $\text{Li}^+(\text{H}_2\text{O})_4$ ) and one bearing excessive negative charge (*i.e.*,  $\text{Li}^+(\text{TFSI}^-)_x$  domain). There is some loose analogy between this structure and the structure of the “soggy sand” electrolytes consisting of the solid-liquid electrolyte with anions adsorbed on the solid resulting in the increased  $t_+$ .<sup>52</sup> One critical question remaining is, are the domains equally dynamic and do  $\text{Li}^+$  ions move together with  $\text{H}_2\text{O}$  or by solvent exchange? To seek an answer, the mean-squared displacements (MSDs) were calculated for  $\text{Li}^+(\text{H}_2\text{O})_n$  not coordinated by TFSI and the  $\text{Li}^+$  coordinated only by TFSI

anions, respectively (Figure 4b). We found that the  $\text{Li}^+$  cations that have no TFSI around diffuse 3 times faster compared to the  $\text{Li}^+$  cations bound by two TFSI on the time scale of a few nanoseconds, which is the lifetime of these solvates. Much faster diffusion of  $\text{Li}^+(\text{H}_2\text{O})_4$  suggests that these solvates are the dominant charge carriers in the solution. Furthermore, the vehicular motion of the  $\text{Li}^+(\text{H}_2\text{O})_n$  is identified as the dominant mechanism, because the  $\text{Li}^+$  moves multiple  $\text{H}_2\text{O}$  sizes (from 5.1 to 6.4  $\text{\AA}$  depending on salt concentration) before it changes its hydration shell on the nanosecond time scale at 298 K. Thus, the  $\text{H}_2\text{O}$ -rich domain in the nano-heterogeneity is responsible for the fast ion transport as well as the high cation-transfer number, with a significant contribution of the  $\text{Li}^+$  vehicular mechanism instead of the solvent exchange mechanism, contrary to the speculation of Yim *et al.*<sup>47</sup> In contrast, in  $(\text{AN})_{2.67}\text{LiTFSI}$  electrolyte the solvent-exchange contribution becomes important at high concentrations as the  $\text{Li}^+$  exchanges each solvent on average as it moves a size of the solvent molecule, which is consistent with the previous discussions.<sup>37</sup> This unusual and interesting transport mechanism in LiTFSI- $\text{H}_2\text{O}$  correlates quite well with the observation of nearly constant activation energies for ion conductivity (Figure 2a), which in turn explains why in typical nonaqueous electrolytes there is such a dramatic change in activation energies with salt concentration due to participation of anion and solvent exchange in the latter. Undoubtedly, the structure and transport mechanisms identified in this work shed valuable light on the tailored design of future electrolyte systems, both aqueous and nonaqueous and either dilute or superconcentrated.

## CONCLUSION

Combining electrochemical, scattering, spectral, and computational techniques, we thoroughly examined the ion solvation and transport in the LiTFSI- $\text{H}_2\text{O}$  system in a wide concentration range from dilute to superconcentrated (21 m) and found that the presence of solvent-separated  $\text{Li}^+$  even at high salt concentrations induces solvation disproportionation of  $\text{Li}^+$  and  $\text{TFSI}^-$  by  $\text{H}_2\text{O}$  molecules, leading to the formation of a liquid structure with nano-heterogeneity. The inhomogeneous distribution of  $\text{Li}^+$  creates two interpenetrating but dynamic nanodomain networks. The TFSI-rich domain relatively immobilizes the anion movement, while the  $\text{Li}^+(\text{H}_2\text{O})_4$  domain serves as a 3D percolating channel for fast  $\text{Li}^+$  transports with high transference number, in sharp contrast to the low transference numbers reported for dilute aqueous electrolytes. It is this ion transport mechanism achieved in superconcentrated aqueous electrolytes that supports diversified cell chemistries at high C-rates. The understanding of this liquid structure of nano-heterogeneity will undoubtedly benefit the future efforts of seeking improved electrochemical storage devices.

## MATERIALS, METHODS, AND MODELING DETAILS

Lithium bis(trifluoromethane sulfonyl) imide ( $\text{LiN}(\text{SO}_2\text{CF}_3)_2$ , LiTFSI) ( $>99\%$ , TCI), lithium hexafluorophosphate ( $>99.9\%$ , BASF), acetonitrile (HPLC grade, Sigma-Aldrich), and carbonate solvents including ethylene carbonate (EC), ethylmethyl carbonate (EMC), and propylene carbonate (PC) (battery grade, BASF) were all used as received. Aqueous and nonaqueous electrolytes were prepared by mixing either LiTFSI or  $\text{LiPF}_6$  with solvents at specified molalities, with the former being made in open ambient and the latter in an Ar-filled glovebox. They were denoted hereafter as LiTFSI- $\text{H}_2\text{O}$ ,

LiTFSI–AN, LiPF<sub>6</sub>–PC, and LiPF<sub>6</sub>–EC/EMC, respectively, followed by corresponding molal numbers. The ionic conductivities were measured with electrochemical impedance spectroscopy (EIS) over a temperature range of –20 to 50 °C for LiTFSI–H<sub>2</sub>O or –20 to 60 °C for nonaqueous systems. A Solartron impedance analyzer equipped with Thermo Scientific Orion conductivity cells was used, whose constants were calibrated with a 0.01 M aqueous KCl standard solution at 25 °C. Each sample was equilibrated in a Tenney oven for at least 1 h before EIS were collected. Viscosity ( $\eta$ ) of the electrolytes was measured on a TA Viscometer AR 2000 at 25 °C with a parallel plate of 40 mm diameter and a 2° cone.

The diffusivity measurements for <sup>1</sup>H, <sup>19</sup>F, and <sup>7</sup>Li nuclei were conducted using pulsed-field-gradient nuclear magnetic resonance (pgf-NMR) experiments. A 400 SB Bruker Avance III spectrometer (9.4 T) equipped with a liquid-state NMR probe with a z-gradient coil (maximum 55 G/cm) was used. For LiTFSI–H<sub>2</sub>O and LiTFSI–AN, 5 mm diameter borosilicate NMR tubes were used. For LiPF<sub>6</sub>–PC and LiPF<sub>6</sub>–EC/EMC, PTFE inserts were used in order to avoid any interaction between the electrolytes and the NMR tubes. Self-diffusion coefficients in LiTFSI–AN, LiPF<sub>6</sub>–PC, and LiPF<sub>6</sub>–EC/EMC were measured at 25 °C using a stimulated echo pulse sequence (with bipolar gradient pulses, spoiler gradients, and a 5 ms Eddy-current delay). Self-diffusion coefficients in LiTFSI–H<sub>2</sub>O were measured at 20 and 30 °C using a double stimulated echo pulse sequence (with bipolar gradient pulses, spoiler gradients, and a 5 ms Eddy-current delay) to suppress convection effects as shown in Tables S2 and S3. Gradient strength was arrayed (16 values, linear increase,  $g = 0\text{--}45$  G/cm) for each experiment, with pulse duration ( $\delta$ ) and diffusion delay ( $\Delta$ ) being 1.5–6 ms and 50–750 ms, respectively. Note that despite faster diffusion of the Li<sup>+</sup>(H<sub>2</sub>O)<sub>4</sub> than Li<sub>+</sub>(TFSI<sup>–</sup>)<sub>n</sub> solvates in MD simulations on the nanosecond time scale, only one average diffusion coefficient was extracted from NMR because on the time scale of NMR measurements (tens to hundreds of ms) the Li<sup>+</sup> motion is homogenized.

All FTIR-ATR spectra were collected using a Nicolet 6700 FT-IR spectrometer (Thermo Scientific) equipped with an ATR accessory unit (specAC). A diamond crystal reflection element was set at an incident beam angle of 45°. Absorbance is obtained from  $-\log(I/I_0)$ , where  $I_0$  is the beam intensity of the background (ATR crystal exposed to Ar gas) and  $I$  is that of the sample on the diamond crystal. More than 128 scans were accumulated with a DLaTGS detector in the 4000–700 cm<sup>–1</sup> range at 2 cm<sup>–1</sup> resolution for each spectrum. All spectra were finally corrected using the advanced ATR correction algorithm in the OMNIC 6.2 software for Thermo Scientific Nicolet FT-IR spectrometers. Principle component analysis (PCA) was used to determine the minimum number of components required in linear combination to explain the sample data variation. A multivariate curve resolution (MCR) using alternating least-squares curve fitting was then used to extract the pure component spectra and their intensities from the sample data. Three components were found and then used to fit the LiTFSI–H<sub>2</sub>O spectra for the TFSI<sup>–</sup> anion. The first component was attributed to the free TFSI<sup>–</sup> anions, which are separated with Li<sup>+</sup> beyond the second solvation shell, and the second component was attributed to the TFSI<sup>–</sup> anions with Li<sup>+</sup> in the second solvation shell, denoted as SSIPs. The third principle mode was attributed to TFSI<sup>–</sup> bound to Li<sup>+</sup>, forming the ion pairs. Further details of FTIR-ATR measurements and PCA-MCR analysis are given in the SI.

SANS measurements were performed at the NIST Center for Neutron Research (NCNR) of the National Institute of Standards and Technology (NIST) on the 30 m SANS instrument located on neutron guide 7 (NG7). Samples were contained in a standard titanium demountable cell with quartz windows and a 1 mm path length. During the experiment the samples were kept at 30 °C using a thermal bath, which allows for temperature control better than  $\pm 0.1$  °C. The incoming neutron wavelength,  $\lambda$ , was 5 Å with a  $\Delta\lambda/\lambda = 14\%$ . Using standard routines,<sup>53</sup> the raw scattering data were corrected for background, empty cell, and sample transmission to get 1D scattering patterns as a function of the momentum transfer  $Q = 4\pi/\lambda \sin[\theta/2]$  ( $\theta$  being the scattering angle).

MD simulations were performed on the LiTFSI–H<sub>2</sub>O system at 298, 333, and 363 K at four concentrations (5.05, 9.25, 13.88, and 20.8 m), which correspond to H<sub>2</sub>O/LiTFSI ratios of 11, 6, 4, and 2.7, respectively. Rounded-up molalities of 5, 9.3, 14, and 21 m are used to refer to these systems in the discussion. Three replicas with different starting configurations were simulated for 21 m LiTFSI in order to establish convergence of MD simulation results with the slowest relaxation. MD simulations utilized a previously developed APPLE&P many-body polarizable force field<sup>54</sup> that was revised for Li<sup>+</sup>TFSI<sup>–</sup> and Li<sup>+</sup>H<sub>2</sub>O along with one additional modification: the Li<sup>+</sup> and TFSI<sup>–</sup> oxygen charges were reduced to make their overall charges 0.92e to enhance ion dynamics.<sup>15</sup>

## ASSOCIATED CONTENT

### Supporting Information

The Supporting Information is available free of charge on the ACS Publications website at DOI: 10.1021/acsnano.7b05664.

Description of IR experiments, MD simulations, conductivity data from experiments, and MD simulations, Walden plot, “ionicity” or dynamic degree of ion dissociation, simulation snapshots, neutron-weighted structure factors from MD simulations and SANS experiments, and the solvate binding energies from quantum chemistry (PDF)

## AUTHOR INFORMATION

### Corresponding Authors

\*E-mail: oleg.a.borodin.civ@mail.mil.

\*E-mail: cswang@umd.edu.

\*E-mail: conrad.k.xu.civ@mail.mil.

### ORCID

Oleg Borodin: 0000-0002-9428-5291

Mallory Gobet: 0000-0001-9735-0741

Jing Peng: 0000-0002-4762-6081

Michael S. Ding: 0000-0002-9302-1032

Chunsheng Wang: 0000-0002-8626-6381

### Author Contributions

<sup>¶</sup>O. Borodin and L. Suo made equal contributions.

### Notes

The authors declare no competing financial interest.

## ACKNOWLEDGMENTS

The collaborative efforts among U.S. Army Research Laboratory (ARL), University of Maryland UMD, and National Institute of Standards and Technology (NIST) were made possible under the Center of Research on Extreme Batteries (CREB), which is part of the ARL Open Campus. Department of Energy Advanced Research Projects Agency - Energy Grant DEAR0000389 to C.W. and K.X. is acknowledged. The NMR measurements conducted at Hunter College were supported by a grant from the U.S. Office of Naval Research, and the NMR facility itself is supported in part by a National Institutes of Health Infrastructure grant (MD007599). M.S. and M.O. acknowledge ORAU postdoc fellowships from the ARL, W911NF-16-2-0187 for M.S. Certain commercial equipment, instruments, or materials are identified in this paper to foster understanding. Such identification does not imply recommendation or endorsement by NIST, nor does it imply that the materials or equipment identified are necessarily the best available for the purpose. S.M. acknowledges financial support by the RISE program at Hunter College (grant GM060665).

## REFERENCES

- (1) Bockris, J. O'M.; Reddy, K. N. *Modern Electrochemistry*, 2nd ed.; Plenum Press: New York, 2000.
- (2) Xu, K. Nonaqueous Liquid Electrolytes for Lithium-Based Rechargeable Batteries. *Chem. Rev.* **2004**, *104*, 4303–4417.
- (3) Angell, C. A.; Liu, C.; Sanchez, E. Rubbery Solid Electrolytes with Dominant Cationic Transport and High Ambient Conductivity. *Nature* **1993**, *362*, 137–139.
- (4) Xu, W.; Wang, L. M.; Angell, C. A. "Polymob"-Lithium Salt Complexes: From Salt-in-Polymer to Polymer-in-Salt Electrolytes. *Electrochim. Acta* **2003**, *48*, 2037–2045.
- (5) Jeong, S. K.; Inaba, M.; Iriyama, Y.; Abe, T.; Ogumi, Z. Electrochemical Intercalation of Lithium Ion within Graphite from Propylene Carbonate Solutions. *Electrochem. Solid-State Lett.* **2003**, *6*, A13–A15.
- (6) Jeong, S. K.; Inaba, M.; Iriyama, Y.; Abe, T.; Ogumi, Z. Interfacial Reactions between Graphite Electrodes and Propylene Carbonate-Based Solutions: Electrolyte-Concentration Dependence of Electrochemical Lithium Intercalation Reaction. *J. Power Sources* **2008**, *175*, 540–546.
- (7) Yoshida, K.; Nakamura, M.; Kazue, Y.; Tachikawa, N.; Tsuzuki, S.; Seki, S.; Dokko, K.; Watanabe, M. Oxidative-Stability Enhancement and Charge Transport Mechanism in Glyme-Lithium Salt Equimolar Complexes. *J. Am. Chem. Soc.* **2011**, *133*, 13121–13129.
- (8) Moon, H.; Mandai, T.; Tatara, R.; Ueno, K.; Yamazaki, A.; Yoshida, K.; Seki, S.; Dokko, K.; Watanabe, M. Solvent Activity in Electrolyte Solutions Controls Electrochemical Reactions in Li-Ion and Li-Sulfur Batteries. *J. Phys. Chem. C* **2015**, *119*, 3957–3970.
- (9) Suo, L. M.; Hu, Y. S.; Li, H.; Armand, M.; Chen, L. Q. A New Class of Solvent-in-Salt Electrolyte for High-Energy Rechargeable Metallic Lithium Batteries. *Nat. Commun.* **2013**, *4*, 1481.
- (10) Lee, J. T.; Zhao, Y.; Thieme, S.; Kim, H.; Oschatz, M.; Borchardt, L.; Magasinski, A.; Cho, W.-I.; Kaskel, S.; Yushin, G. Sulfur-Infiltrated Micro- and Mesoporous Silicon Carbide-Derived Carbon Cathode for High-Performance Lithium Sulfur Batteries. *Adv. Mater.* **2013**, *25*, 4573–4579.
- (11) Yamada, Y.; Furukawa, K.; Sodeyama, K.; Kikuchi, K.; Yaegashi, M.; Tateyama, Y.; Yamada, A. Unusual Stability of Acetonitrile-Based Superconcentrated Electrolytes for Fast-Charging Lithium-Ion Batteries. *J. Am. Chem. Soc.* **2014**, *136*, 5039–5046.
- (12) Wang, J.; Yamada, Y.; Sodeyama, K.; Chiang, C. H.; Tateyama, Y.; Yamada, A. Superconcentrated Electrolytes for a High-Voltage Lithium-Ion Battery. *Nat. Commun.* **2016**, *7*, 12032.
- (13) McOwen, D. W.; Seo, D. M.; Borodin, O.; Vatamanu, J.; Boyle, P. D.; Henderson, W. A. Concentrated Electrolytes: Decrypting Electrolyte Properties and Reassessing Al Corrosion Mechanisms. *Energy Environ. Sci.* **2014**, *7*, 416–426.
- (14) Kuhnle, R. S.; Reber, D.; Remhof, A.; Figi, R.; Bleiner, D.; Battaglia, C. "Water-in-Salt" Electrolytes Enable the Use of Cost-Effective Aluminum Current Collectors for Aqueous High-Voltage Batteries. *Chem. Commun.* **2016**, *52*, 10435–10438.
- (15) Suo, L.; Borodin, O.; Gao, T.; Olguin, M.; Ho, J.; Fan, X.; Luo, C.; Wang, C.; Xu, K. Water-in-Salt" Electrolyte Enables High-Voltage Aqueous Lithium-Ion Chemistries. *Science* **2015**, *350*, 938–943.
- (16) Wang, F.; Lin, Y.; Suo, L.; Fan, X.; Gao, T.; Yang, C.; Han, F.; Qi, Y.; Xu, K.; Wang, C. Stabilizing High Voltage LiCoO<sub>2</sub> Cathode in Aqueous Electrolyte with Interphase-Forming Additive. *Energy Environ. Sci.* **2016**, *9*, 3666–3673.
- (17) Yamada, Y.; Usui, K.; Sodeyama, K.; Ko, S.; Tateyama, Y.; Yamada, A. Hydrate-Melt Electrolytes for High-Energy-Density Aqueous Batteries. *Nat. Energy* **2016**, *1*, 16129.
- (18) Suo, L.; Han, F.; Fan, X.; Liu, H.; Xu, K.; Wang, C. "Water-in-Salt" Electrolytes Enable Green and Safe Li-Ion Batteries for Large Scale Electric Energy Storage Applications. *J. Mater. Chem. A* **2016**, *4*, 6639–6644.
- (19) Ramanujapuram, A.; Gordon, D.; Magasinski, A.; Ward, B.; Nitta, N.; Huang, C.; Yushin, G. Degradation and Stabilization of Lithium Cobalt Oxide in Aqueous Electrolytes. *Energy Environ. Sci.* **2016**, *9*, 1841.
- (20) Kuhnle, R.-S.; Reber, D.; Battaglia, C. A High-Voltage Aqueous Electrolyte for Sodium-Ion Batteries. *ACS Energy Lett.* **2017**, *2*, 2005–2006.
- (21) Suo, L.; Borodin, O.; Wang, Y.; Rong, X.; Sun, W.; Fan, X.; Xu, S.; Schroeder, M. A.; Cresce, A. V.; Wang, F.; Yang, C.; Hu, Y.-S.; Xu, K.; Wang, C. Water-in-Salt" Electrolyte Makes Aqueous Sodium-Ion Battery Safe, Green, and Long-Lasting. *Adv. Energy Mater.* **2017**, *1701189*.
- (22) Gordon, D.; Wu, M. Y.; Ramanujapuram, A.; Benson, J.; Lee, J. T.; Magasinski, A.; Nitta, N.; Huang, C.; Yushin, G. Enhancing Cycle Stability of Lithium Iron Phosphate in Aqueous Electrolytes by Increasing Electrolyte Molarity. *Adv. Energy Mater.* **2016**, *6*, 1501805.
- (23) Yang, C.; Chen, J.; Qing, T.; Fan, X.; Sun, W.; von Cresce, A.; Ding, M. S.; Borodin, O.; Vatamanu, J.; Schroeder, M. A.; Eidson, N.; Wang, C.; Xu, K. 4.0 V Aqueous Li-Ion Batteries. *Joule* **2017**, *1*, 122–132.
- (24) Suo, L.; Borodin, O.; Sun, W.; Fan, X.; Yang, C.; Wang, F.; Gao, T.; Ma, Z.; Schroeder, M.; von Cresce, A.; Russell, S. M.; Armand, M.; Angell, A.; Xu, K.; Wang, C. Advanced High-Voltage Aqueous Lithium-Ion Battery Enabled by "Water-in-Bisalt" Electrolyte. *Angew. Chem., Int. Ed.* **2016**, *55*, 7136–7141.
- (25) von Cresce, A.; Xu, K. Preferential Solvation of Li<sup>+</sup> Directs Formation of Interphase on Graphitic Anode. *Electrochem. Solid-State Lett.* **2011**, *14*, A154–A156.
- (26) Xu, K.; Cresce, A. V. Li<sup>+</sup>-Solvation/Desolvation Dictates Interphasial Processes on Graphitic Anode in Li Ion Cells. *J. Mater. Res.* **2012**, *27*, 2327–2341.
- (27) von Wald Cresce, A.; Gobet, M.; Borodin, O.; Peng, J.; Russell, S. M.; Wikner, E.; Fu, A.; Hu, L.; Lee, H.-S.; Zhang, Z.; Yang, X.-Q.; Greenbaum, S.; Amine, K.; Xu, K. Anion Solvation in Carbonate-Based Electrolytes. *J. Phys. Chem. C* **2015**, *119*, 27255–27264.
- (28) Seo, D. M.; Borodin, O.; Han, S.-D.; Ly, Q.; Boyle, P. D.; Henderson, W. A. Electrolyte Solvation and Ionic Association. I. Acetonitrile-Lithium Salt Mixtures: Intermediate and Highly Associated Salts. *J. Electrochem. Soc.* **2012**, *159*, A553–A565.
- (29) von Wald Cresce, A.; Borodin, O.; Xu, K. Correlating Li<sup>+</sup> Solvation Sheath Structure with Interphasial Chemistry on Graphite. *J. Phys. Chem. C* **2012**, *116*, 26111–26117.
- (30) Vatamanu, J.; Borodin, O. Ramifications of Water-in-Salt Interfacial Structure at Charged Electrodes for Electrolyte Electrochemical Stability. *J. Phys. Chem. Lett.* **2017**, *8*, 4362–4367.
- (31) Mason, P. E.; Ansell, S.; Neilson, G. W.; Rempe, S. B. Neutron Scattering Studies of the Hydration Structure of Li<sup>+</sup>. *J. Phys. Chem. B* **2015**, *119*, 2003–2009.
- (32) Kameda, Y.; Miyazaki, T.; Otomo, T.; Amo, Y.; Usuki, T. Neutron Diffraction Study on the Structure of Aqueous Lino<sub>3</sub> Solutions. *J. Solution Chem.* **2014**, *43*, 1588–1600.
- (33) Ding, M. S.; von Cresce, A.; Xu, K. Conductivity, Viscosity, and their Correlation of a Super-Concentrated Aqueous Electrolyte. *J. Phys. Chem. C* **2017**, *121*, 2149–2153.
- (34) Wang, F.; Suo, L.; Liang, Y.; Yang, C.; Han, F.; Gao, T.; Sun, W.; Wang, C. Spinel LiNi<sub>0.5</sub>Mn<sub>1.5</sub>O<sub>4</sub> Cathode for High-Energy Aqueous Lithium-Ion Batteries. *Adv. Energy Mater.* **2017**, *7*, 1600922.
- (35) Perron, G.; Brouillette, D.; Desnoyers, J. E. Comparison of the Thermodynamic and Transport Properties of Lithium Bis-(trifluoromethylsulfonyl)imide (LiTFSI) with LiClO<sub>4</sub> and Bu<sub>4</sub>NBr in Water at 25 Degrees C. *Can. J. Chem.* **1997**, *75*, 1608–1614.
- (36) Hirayama, H.; Tachikawa, N.; Yoshii, K.; Watanabe, M.; Katayama, Y. Ionic Conductivity and Viscosity of Solvate Ionic Liquids Composed of Glymes and Excess Lithium Bis-(trifluoromethylsulfonyl)amide. *Electrochemistry* **2015**, *83*, 824–827.
- (37) Seo, D. M.; Borodin, O.; Balogh, D.; O'Connell, M.; Ly, Q.; Han, S.-D.; Passerini, S.; Henderson, W. A. Electrolyte Solvation and Ionic Association III. Acetonitrile-Lithium Salt Mixtures—Transport Properties. *J. Electrochem. Soc.* **2013**, *160*, A1061–A1070.
- (38) Ding, M. S.; Jow, T. R. Conductivity and Viscosity of PC-DEC and PC-EC Solutions of LiPF<sub>6</sub>. *J. Electrochem. Soc.* **2003**, *150*, A620–A628.

(39) Ueno, K.; Yoshida, K.; Tsuchiya, M.; Tachikawa, N.; Dokko, K.; Watanabe, M. Glyme-Lithium Salt Equimolar Molten Mixtures: Concentrated Solutions or Solvate Ionic Liquids? *J. Phys. Chem. B* **2012**, *116*, 11323–11331.

(40) Qian, J.; Henderson, W. A.; Xu, W.; Bhattacharya, P.; Engelhard, M.; Borodin, O.; Zhang, J.-G. High Rate and Stable Cycling of Lithium Metal Anode. *Nat. Commun.* **2015**, *6*, 6362.

(41) Zhang, C.; Ueno, K.; Yamazaki, A.; Yoshida, K.; Moon, H.; Mandai, T.; Umabayashi, Y.; Dokko, K.; Watanabe, M. Chelate Effects in Glyme/Lithium Bis(trifluoromethanesulfonyl)amide Solvate Ionic Liquids. I. Stability of Solvate Cations and Correlation with Electrolyte Properties. *J. Phys. Chem. B* **2014**, *118*, 5144–5153.

(42) Watanabe, Y.; Kinoshita, S. I.; Wada, S.; Hoshino, K.; Morimoto, H.; Tobishima, S. I. Electrochemical Properties and Lithium Ion Solvation Behavior of Sulfone-Ester Mixed Electrolytes for High-Voltage Rechargeable Lithium Cells. *J. Power Sources* **2008**, *179*, 770–779.

(43) Takeuchi, M.; Kameda, Y.; Umabayashi, Y.; Ogawa, S.; Sonoda, T.; Ishiguro, S. I.; Fujita, M.; Sano, M. Ion-Ion Interactions of LiPF<sub>6</sub> and LiBF<sub>4</sub> in Propylene Carbonate Solutions. *J. Mol. Liq.* **2009**, *148*, 99–108.

(44) Xu, K. Electrolytes and Interphases in Li-Ion Batteries and Beyond. *Chem. Rev.* **2014**, *114*, 11503–11618.

(45) Zugmann, S.; Fleischmann, M.; Amereller, M.; Gschwind, R. M.; Wiemhofer, H. D.; Gores, H. J. Measurement of Transference Numbers for Lithium Ion Electrolytes *via* four Different Methods, a Comparative Study. *Electrochim. Acta* **2011**, *56*, 3926–3933.

(46) Dai, H. L.; Zawodzinski, T. A. Determination of Lithium Ion Transference Numbers by Electrophoretic Nuclear Magnetic Resonance. *J. Electrochem. Soc.* **1996**, *143*, L107–L109.

(47) Yim, C.-H.; Tam, J.; Soboleski, H.; Abu-Lebdeh, Y. On the Correlation between Free Volume, Phase Diagram and Ionic Conductivity of Aqueous and Non-Aqueous Lithium Battery Electrolyte Solutions over a Wide Concentration Range. *J. Electrochem. Soc.* **2017**, *164*, A1002–A1011.

(48) Yasuo, K.; Shun, S.; Hidekazu, E.; Takeshi, U.; Osamu, U. The Short-Range Structure around Li<sup>+</sup> in Highly Concentrated Aqueous LiBr Solutions. *Bull. Chem. Soc. Jpn.* **1997**, *70*, 47–53.

(49) Borodin, O.; Smith, G. D. Mechanism of Ion Transport in Amorphous Poly(ethylene Oxide)/LiTFSI from Molecular Dynamics Simulations. *Macromolecules* **2006**, *39*, 1620–1629.

(50) Mao, G.; Saboungi, M.-L.; Price, D. L.; Armand, M. B.; Howells, W. S. Structure of Liquid Peo-LiTFSI Electrolyte. *Phys. Rev. Lett.* **2000**, *84*, 5536–5539.

(51) Borodin, O.; Gorecki, W.; Smith, G. D.; Armand, M. Molecular Dynamics Simulation and Pulsed-Field Gradient NMR Studies of Bis(fluorosulfonyl)imide (FSI) and Bis[(trifluoromethyl)sulfonyl]imide (TFSI)-Based Ionic Liquids. *J. Phys. Chem. B* **2010**, *114*, 6786–6798.

(52) Popovic, J.; Hasegawa, G.; Moudrakovski, I.; Maier, J. Infiltrated Porous Oxide Monoliths as High Lithium Transference Number Electrolytes. *J. Mater. Chem. A* **2016**, *4*, 7135–7140.

(53) Kline, S. R. Reduction and Analysis of Sans and Usans Data Using Igor Pro. *J. Appl. Crystallogr.* **2006**, *39*, 895–900.

(54) Borodin, O. Polarizable Force Field Development and Molecular Dynamics Simulations of Ionic Liquids. *J. Phys. Chem. B* **2009**, *113*, 11463–11478.